CANADIAN JOURNAL OF EXPLORATION GEOPHYSICS
VOL. 26, NOS. 1 & 2 (DECEMBER 1990), P. 7-16

A 9-COMPONENT REFRACTION SEISMIC EXPERIMENT[1]

DON C. LAWTON[2]

ABSTRACT

A 9-component refraction seismic survey was conducted near Calgary, Canada. A steel hammer striking a wooden beam was used to generate *S*-waves, and a Betsy™ seisgun was used to produce *P*-waves. Data were recorded using single, three-component geophones, and good quality *P*, *SV* and *SH* head-wave data were acquired. The water table was found to produce strong *P*-wave refracted arrivals but was transparent to *S*-waves. V_p/V_s below the water table was greater than 8. Static corrections to the base of the weathered layer at a depth of 20 m were 42 ms for *P-P* data, 89 ms for *P-SV* data, and 136 ms for *SH-SH* data. Weak *S*-wave velocity anisotropy was found in the unweathered Cretaceous clastic bedrock.

INTRODUCTION

Recently, there has been increased interest in the use of multicomponent reflection seismic data for the exploration and development of hydrocarbon reservoirs. In particular, three-component recording has enabled *S*-wave reflection data to be collected (Domenico and Danbom, 1986). These data are, in the absence of subsurface anisotropy, either pure shear (*SH-SH*) or mode-converted (*P-SV*), recorded with transverse (cross-line) or radial (in-line) geophones, respectively.

One of the most important corrections applied to *S*-wave data is the static correction, which is necessary to remove the effects of topography and variations in near-surface velocity (weathering). In Alberta, the weathering statics problem is particularly severe due to the irregular thickness of glacial sediments which blanket most of the western Canada basin. This has a direct impact on the recording and processing of *S*-wave reflection data because the velocity of *S*-waves in the weathering layer is much less than that of *P*-waves (Wiest and Edelman, 1984; Anno, 1987), resulting in much larger static corrections for *S*-wave data than for *P*-wave data. Hence, weathering static corrections for *SH-SH* surveys are greater than those for *P-SV* surveys. This is because, in the former case, downgoing as well as upgoing waves are *S*-waves, whereas in the latter case, the downgoing wave is a *P*-wave, with consequently a smaller associated static correction.

Weathering statics in conventional *P*-wave data processing are generally computed by the analysis of head-wave arrivals (first breaks). Refraction analysis is undertaken using delay-time methods (Gardner, 1939; Hagedoorn, 1959; Hawkins, 1961; Palmer, 1980; Lawton, 1989) or inversion techniques (Hampson and Russell, 1984; Chiu and Law, 1989) to provide the depth and velocity structure of the near-surface layers, from which reflection static corrections can be computed.

A significant problem with the processing of *P-SV* reflection data is the difficulty in evaluating the receiver static corrections by refraction analysis. This is because a significant amount of *P*-wave energy is recorded by the radial-component receivers, and *SV* head waves (either source-generated or mode-converted) are obscured by the multiple *P*-wave refractions which arrive earlier. Hence the travel-time of the *SV* head wave is often difficult to pick. A common practice is to estimate the *S*-wave weathering static correction directly from the *P*-wave weathering static correction. Typically, $V_p/V_s = 2$ is assumed so that, for vertical raypaths and a common datum, the ratio of *P-SV* static corrections to *P-P* static corrections will be 1.5.

The purpose of this study was to evaluate the *P*-wave and *S*-wave velocity structure for surficial glacial sediments near Calgary and to determine the relative magnitudes of *P*-wave and *S*-wave weathering static corrections. This was achieved by undertaking an experimental multicomponent refraction survey.

FIELD PROGRAM

The multicomponent refraction test was undertaken during the 1989 University of Calgary Geophysics Field School, which was held at Jumping Pound (Twp 26, Rge 5

[1]Presented at the C.S.E.G. National Convention, Calgary, Alberta, May 17, 1990. Manuscript received by the Editor June 25, 1990; revised manuscript received October 5, 1990.

[2]Department of Geology and Geophysics, The University of Calgary, Calgary, Alberta T2N 1N4

Collection of the data was assisted by students and staff from the Department of Geology and Geophysics, University of Calgary. I wish to thank Mr. Scott Graham from Unocal Canada for providing us with the components for the shear-wave source. The study was supported by the Consortium for Research in Elastic Wave Exploration Seismology (CREWES) project at the University of Calgary.

W5), about 30 km west of Calgary. At the site, a thin layer of glacial sediment covers sandstones and mudstones of the Cretaceous Belly River Formation. Near-surface conditions at this site are typical for the southwestern part of the western Canada sedimentary basin.

Two different sources were used for the test. The *S*-wave source consisted of an 80 kg steel hammer which struck the end of a 0.3 m x 0.3 m wooden beam 3 m in length. The beam was held down by a 1-ton cable truck and anchored to the ground by strips of angle iron. The hammer length was adjustable and pivoted from a wooden support beam which was lashed across the top of the cage on the cable truck. Figure 1 shows a schematic diagram of the active elements of the *S*-wave source, and Figure 2a shows a photograph of the source in operation. For each shot, the hammer was raised manually to a fixed height, then released upon a verbal command. Time zero was established by a trigger geophone placed on the source beam. Bouncing of the hammer on the end of the beam was prevented by catching it with a rope after the first impact (Figure 2a). The *P*-wave source used in the experiment was the Betsy™ seisgun (Varsek and Lawton, 1985). It fired electric shells and was triggered using an Input-Output blaster.

Single, three-component OYO geophones were used to acquire the data, with a geophone separation of 15 m. The geophone elements have a resonant frequency of 10 Hz and the geophone case is equipped with a levelling bubble and arrows for orientation, as shown by the photograph in Figure 2b. To minimize wind noise, the geophones were buried below the ground surface. A 48-trace DFS-III system was used to record the data, allowing 16 live ground stations for the active spread. Figure 3 shows a diagram of the field acquisition geometry.

Reciprocal records into a single spread were acquired in the experiment, with source locations coincident with the first and last geophones of the spread (Figure 3). At each source location, 5 data sets were obtained, consisting of 1 set of records using the *P*-wave source and 4 sets of records using the *S*-wave source. Each data set consisted of 15 individual records which were vertically stacked to enhance the signal-to-noise ratio. The *S*-wave source was oriented in two orthogonal modes: transverse to the receiver spread to generate *SH*-waves and in-line with the spread to produce *SV*-waves (Figure 3). In each mode, separate data sets were acquired (e.g., *SH*+ and *SH*–) with the hammer striking opposite ends of the beam.

After the multicomponent refraction experiment had been completed, a conventional *P*-wave reflection program was undertaken in the study area along a line which included the test refraction spread. The reflection program was 12-fold and the source was 2 kg of dynamite in drill holes 18 to 20 m deep. First-break interpretation of records from this program provided the *P*-wave velocity of the Cretaceous bedrock, and drillers' logs were used to test the depth interpretation from the multicomponent refraction survey.

Data Reduction

After demultiplexing the data, the 15 records from each data set were vertically summed. It was found that the time break was not consistent, but varied by up to 10 ms from shot to shot, due to difficulties in firmly securing the trigger geophone to the wooden beam. For all data sets, the first record from that set was selected as the pilot record and each remaining record in the data set was cross-correlated

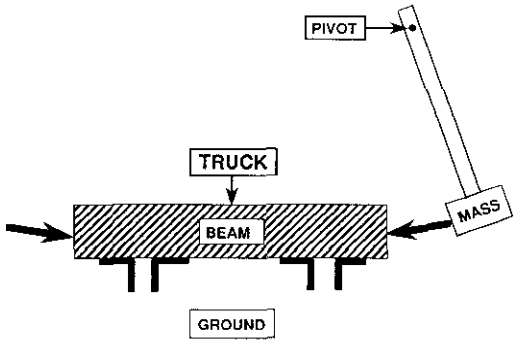

Fig. 1. Schematic diagram of the *S*-wave source. The beam is held in place by a truck (not shown) which also supports the pivot point for the mass.

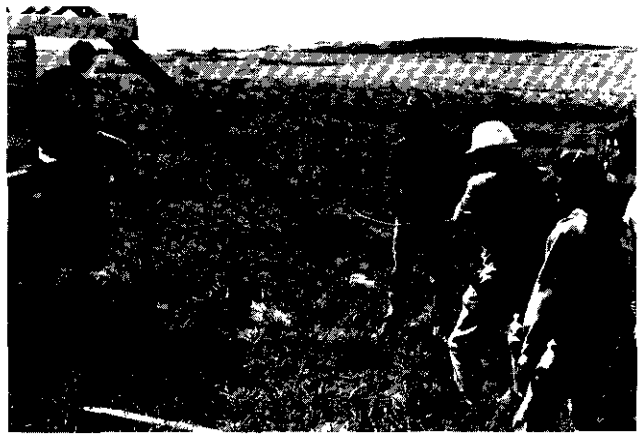

Fig. 2. Photographs of the *S*-wave refraction test field operations: **(a)** source showing pendulum mass; **(b)** 3-component OYO geophone showing levelling bubble and orientation arrows.

with the pilot record. The lag for maximum correlation was then applied as a bulk shift to the record before summing.

The *S*-wave source invariably created some *P*-wave energy during operation, because the wooden beam was rarely perfectly level and the hammer was not necessarily exactly orthogonal to the beam when it struck the end. The signal-to-noise ratio of the *S*-wave data was enhanced considerably by subtracting the data sets acquired with the hammer striking the opposite ends of the beam while in the same mode (*SH* or *SV*). The *S*-wave energy has opposite polarity between the data sets, whereas the *P*-wave energy has the same polarity (Hasbrouk, 1987). Thus, when the data sets are subtracted, *S*-wave data are enhanced, whereas *P*-wave energy is attenuated. Conversely, if the records are summed, then the *P*-wave data are enhanced and *S*-wave energy is attenuated. This procedure for *P* and *S* wave-field separation is illustrated in Figure 4, using traces recorded with a transverse geophone and an *SH* source orientation.

Prior to subtraction, the record pairs were cross-correlated to extract any residual time-break error, and the average amplitudes of the records were also normalised. After subtraction, the total data set was reduced to 6 records, consisting of 3 records from each end of the spread for *P*, *SH* and *SV* sources.

Results

Figure 5 shows an example of the final record obtained for an *SH* source positioned at the eastern source point (Figure 3). For clarity of display, the 48-trace record was decomposed into three separate 16-trace records containing the vertical, radial and transverse components, as labelled on the Figure. The data in Figure 5a have been trace-equalised and scaled using a 300 ms sliding window. As expected, the transverse component contains the cleanest *S*-wave refracted arrivals since this record was obtained with an *SH* source. However, there appears to be considerable head wave energy (*P* and *S*) on both the vertical and radial components. Figure 5b shows the same data displayed with no trace balancing or AGC applied, so that the relative amplitude levels between the three components can be better appreciated. This display shows that the transverse component has indeed recorded the highest amplitude events, although there is a significant signal level on the radial channel. This could be due to orientation errors in positioning the geophone, near-surface *S*-wave anisotropy, or cross talk between the horizontal elements of the geophone. Figure 5b also shows that the signal level on the vertical channel is actually much less than on either of the two horizontal channels.

Figure 6 contains the same data as Figure 5, and shows a comparison between subtracting and adding the *S*-wave data sets recorded with the same source mode (*SH*) but with opposite directions of excitation. Figure 6a shows results after subtracting the *SH*+ and *SH*– records, whereas Figure 6b shows the data after adding the records. This figure illustrates clearly the effectiveness of the subtraction and addition processes for *P* and *S* wave-field separation.

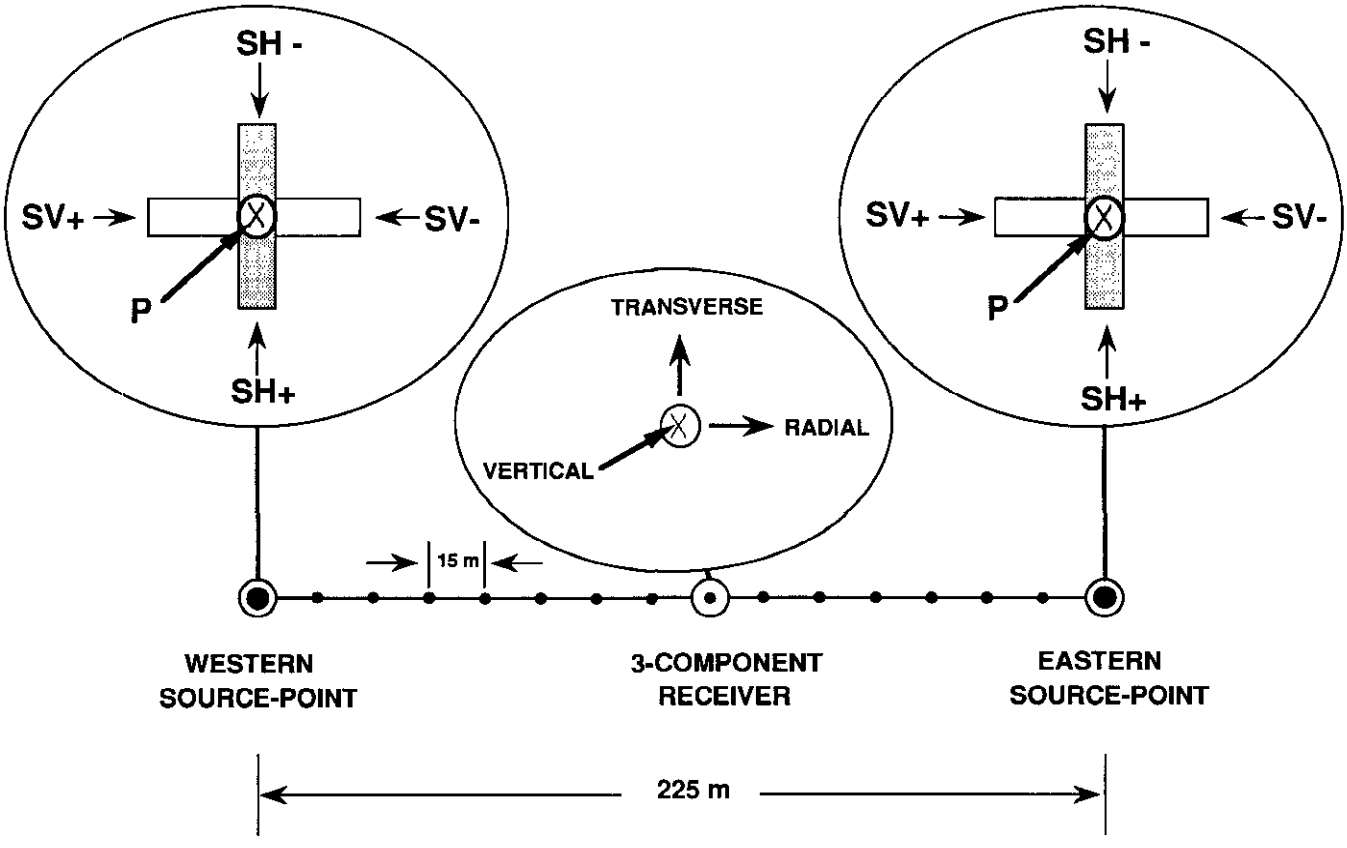

Fig. 3. Field set-up and acquisition geometry of the 9-component refraction spread.

Near-Surface Velocity Structure

The full 9-component data set (3 source orientations x 3 receiver orientations) from the eastern source point is shown in Figure 7. Interpretation of the data to obtain the near-surface *P*- and *S*-wave velocity structure was based on the 3 records, highlighted in boxes, along the diagonal in Figure 7. These are the highest quality records because they have matched source-receiver orientations. The off–diagonal records have weaker first-break energy because the source and receiver orientations are not matched. As discussed above, energy detected on mismatched components may be due simply to orientation errors in the source or geophones, or it may be indicative of cross dip of the refractor or near-surface velocity anisotropy. Further analysis of these records will be undertaken in a follow-up paper.

The subset of diagonal records from Figure 7, along with similar records from the western source point, are interpreted in Figures 8a and 8b, respectively. Direct and refracted arrivals are marked on each record. The vertical-component records show *P*-wave refracted arrivals across all traces, whereas the transverse-component and radial-component records show a distinct crossover at an offset of about 60 m (4 traces).

Because of the limited source-receiver offset range and the lack of apparent refractor structure for both *P* and *S* data, a slope and intercept time interpretation was undertaken (Gardner, 1939). Velocities and layer thicknesses, averaged from reciprocal records, are summarised in Figure 9 for both the *S*-wave and *P*-wave data. Errors in the velocities are estimated to be less than +/– 40 m/s, based on the scatter in first-break traveltimes. Subsequent errors in the depths are estimated to be less than +/– 3 m. A determination of the *SV* velocity in the surface layer was not obtainable from the radial-component records because of contamination of the near-offset data by *P*-wave energy. This is considered to be caused by a probable asymmetric, in-line radiation pattern of *SV* energy from the *S*-wave source when oriented in the radial direction. However, this was indeed fortuitous because no direct *P*-wave arrivals were observed on the vertical-component records, and it enabled the *P*-wave velocity of 600 m/s to be determined for the surface layer (Figure 9). This is considered to be only an average value for the top 10 m, and it is probable that there is a vertical velocity gradient in this layer.

For the *P*-wave results in Figure 9, the thickness of the second layer and the velocity of the third layer (3150 +/– 50 m/s) were determined from the analysis of first breaks from records obtained from the conventional *P*-wave seismic

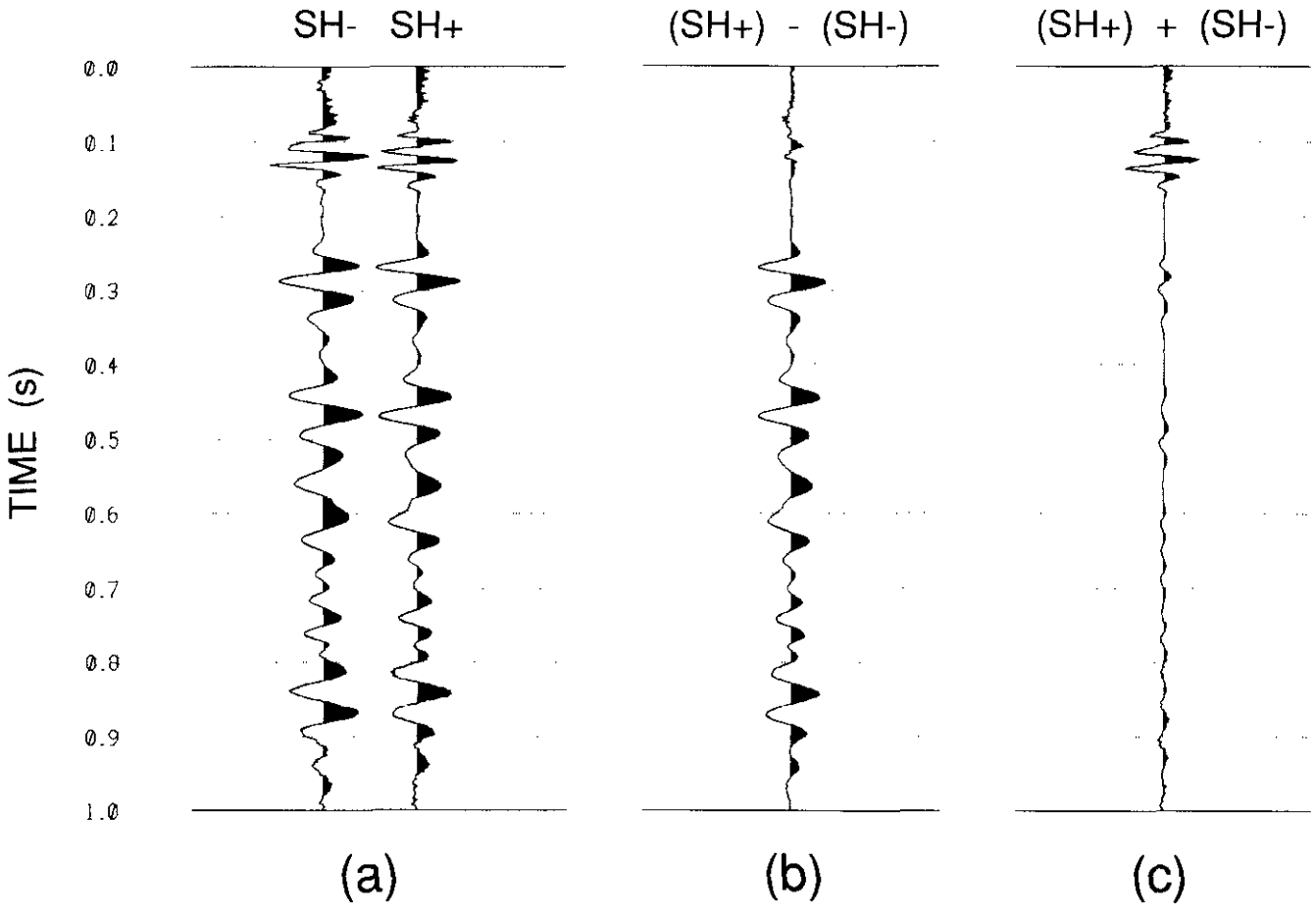

Fig. 4. Illustration of *P* and *S* wave-field separation technique by subtraction and addition of traces recorded with opposite directions of source excitation (*SH* mode): **(a)** raw traces; **(b)** subtracted traces (*S*-wave enhancement); **(c)** added traces (*P*-wave enhancement).

program. Figure 10 contains two reciprocal records from this program, showing the overlap with the experimental refraction spread. The thickness and velocity data were calculated using the plus-minus method of Hagedoorn (1959).

Discussion

Figure 9 shows clearly that the shallow velocity structure for *P*-waves and *S*-waves is very different. The increase in *P*-wave velocity at a depth of 10 m coincides with the water table, an interpretation which was later confirmed by the shot hole drillers' logs from the conventional *P*-wave reflection program. Since no *S*-wave refracted arrival was recorded from the water table, no increase in *S*-wave velocity is evident at this interface, a result consistent with velocity studies of porous rocks by Domenico (1976) and Gregory (1976). Note that V_p/V_s increases to a value greater than 8 in the water-saturated, weathered zone. These results are similar to those described by Wiest and Edelmann (1984) for a multicomponent refraction survey in northern Germany. Also, for head waves along the deepest refractor, the *SV*-wave velocity is about 10 percent lower than the *SH*-wave velocity, possibly indicating that the unweathered Cretaceous sediments below the test line are weakly anisotropic.

The differences between the near-surface *P*-wave and *S*-wave velocity structure has a significant impact on weathering static corrections. Figure 9 shows the magnitude of the static corrections which would be applied in *P-P*, *P-SV* and *SH-SH* reflection surveys. These values were computed on the basis of vertical travel paths and to a datum at a depth of 20 m below surface. The total weathering static for the *SH-SH* survey is 3.5 times greater than the *P-P* static, and the *P-SV* static is over twice the value of the *P-P* static correction.

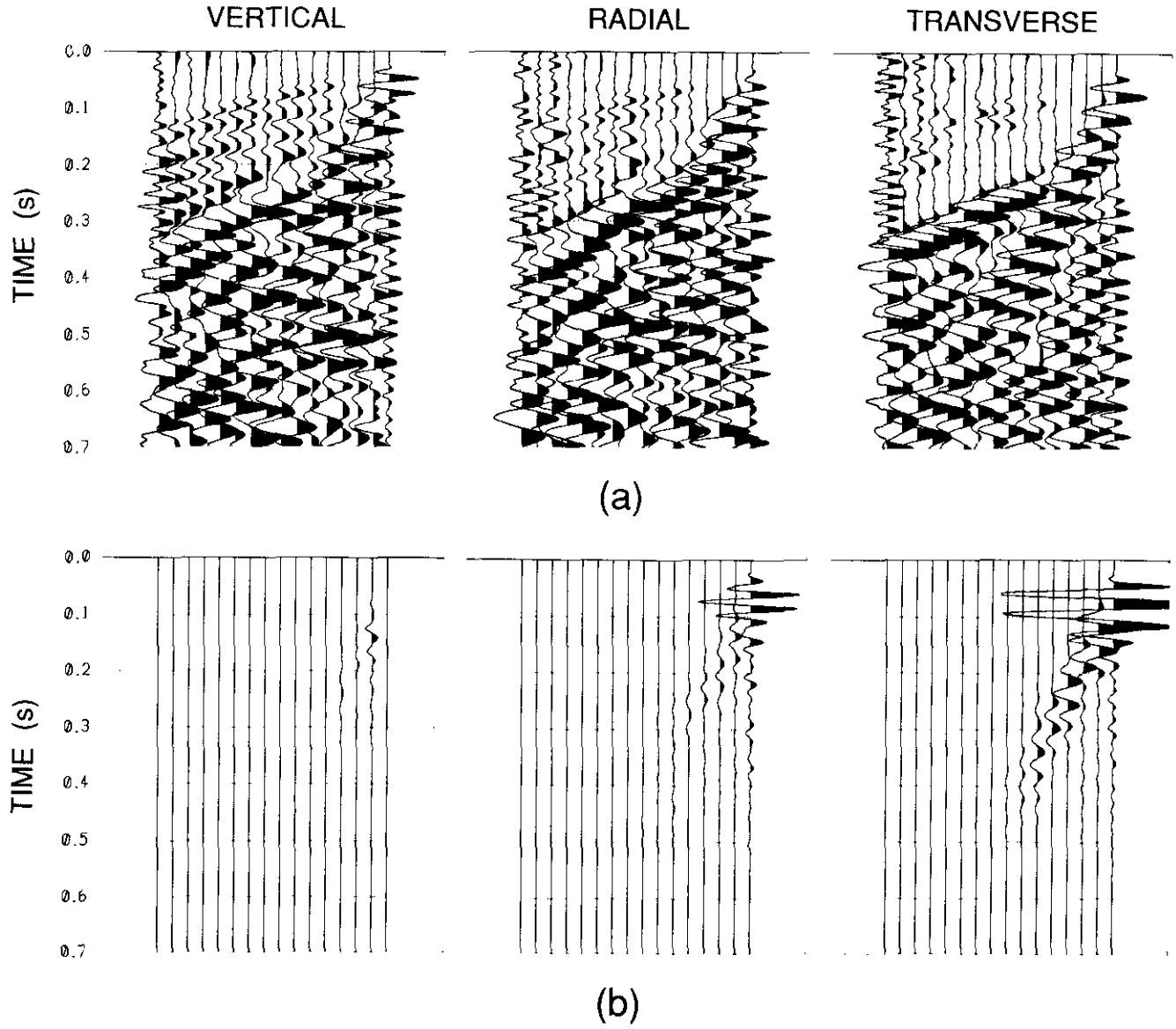

Fig. 5. Example of a 3-component record obtained with the *S*-wave source operating in the *SH* mode: **(a)** data scaled with a 300 ms AGC operator; **(b)** data unscaled, showing true relative amplitude between traces and geophone components.

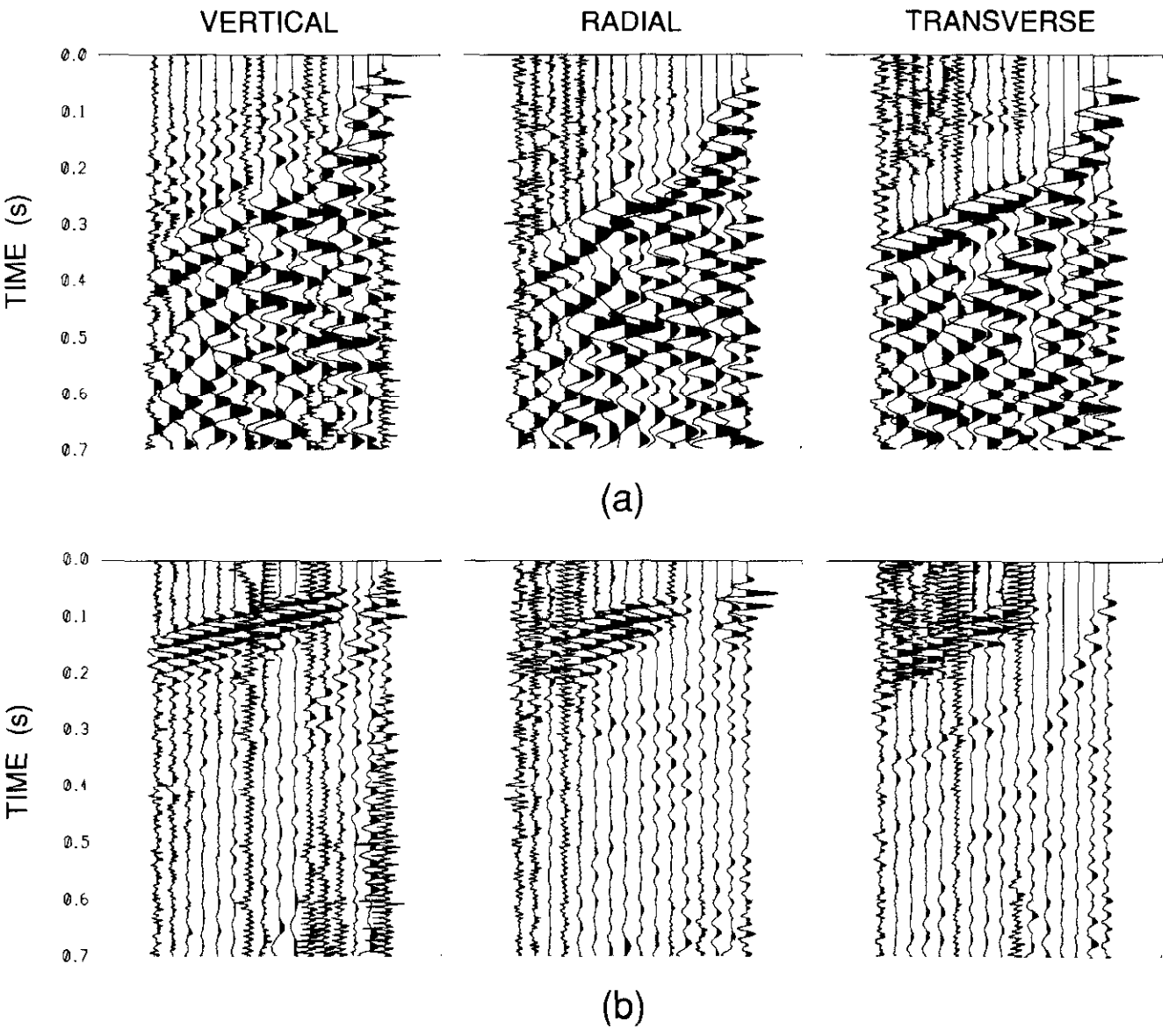

Fig. 6. The same records as in Figure 5 but showing the S and P wave-field separation through the subtraction **(a)** and addition **(b)** of $SH+$ and $SH-$ records, respectively.

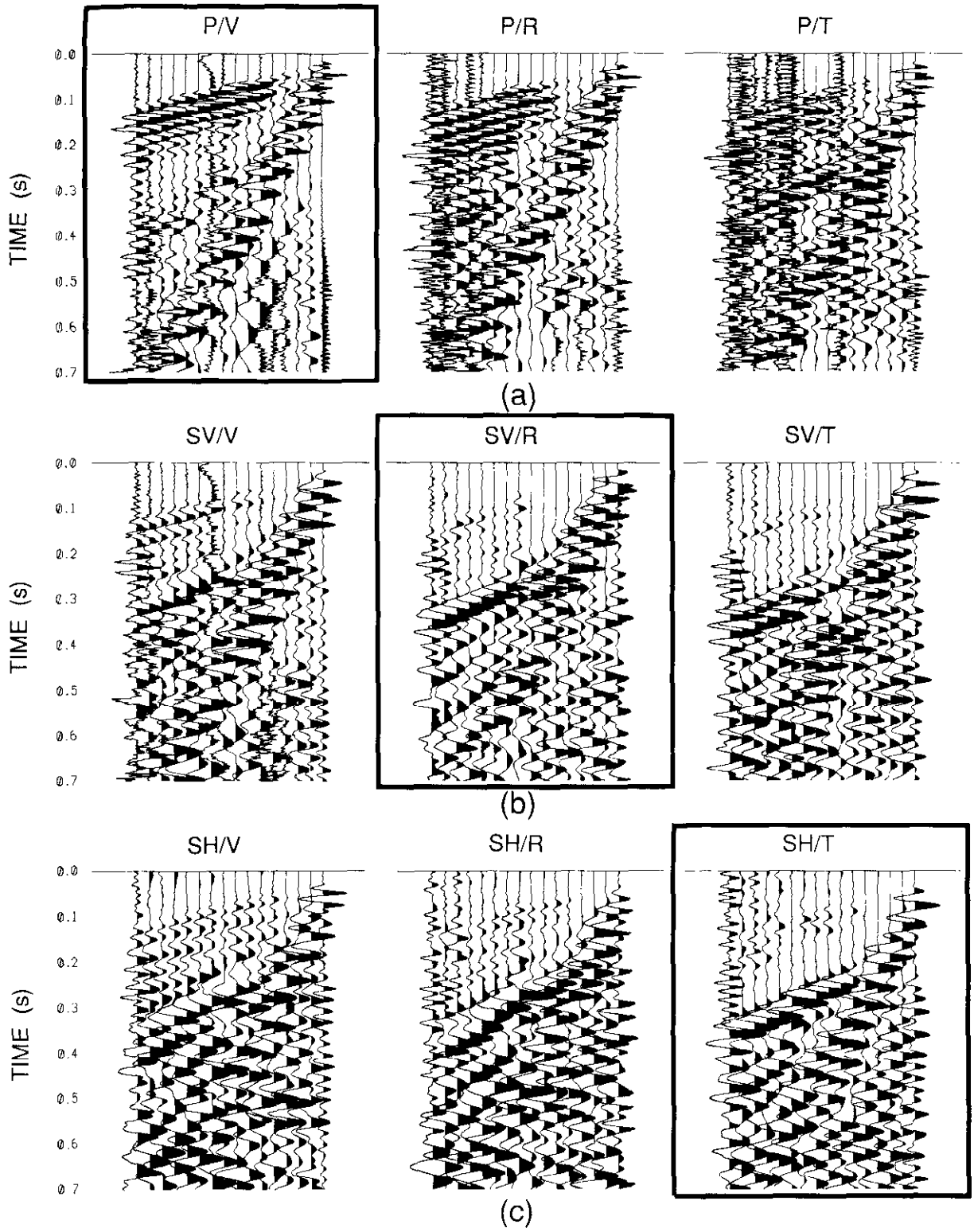

Fig. 7. The processed 9-component data set recorded with the source located at the eastern source point: **(a)** *P*-source mode; **(b)** *SV*-source mode; **(c)** *SH*-source mode. The boxed records along the diagonal show records with matched source and receiver orientations.

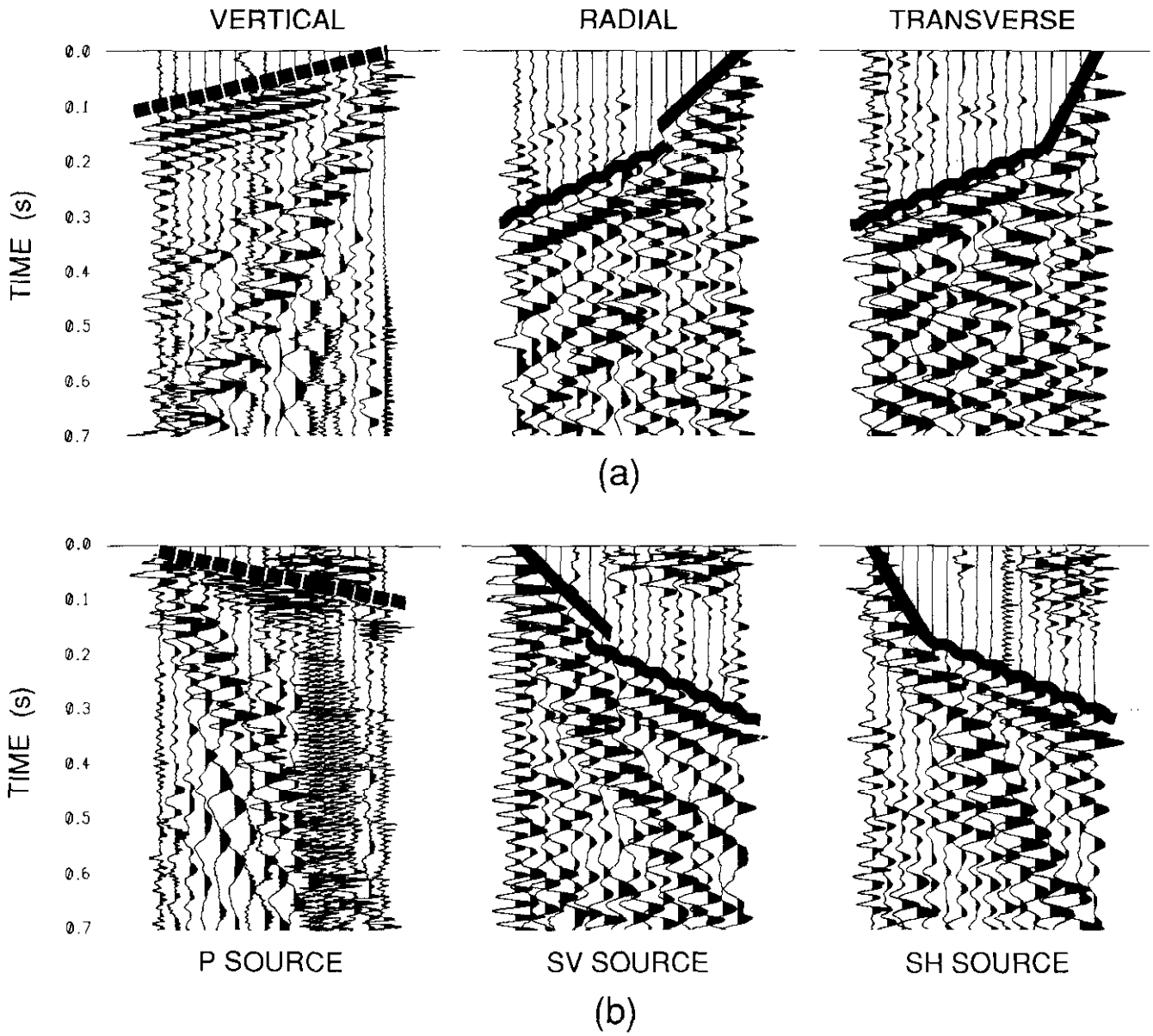

Fig. 8. Interpreted records for matched source and receiver orientations, with direct and refracted arrivals marked: **(a)** eastern source point; **(b)** western source point.

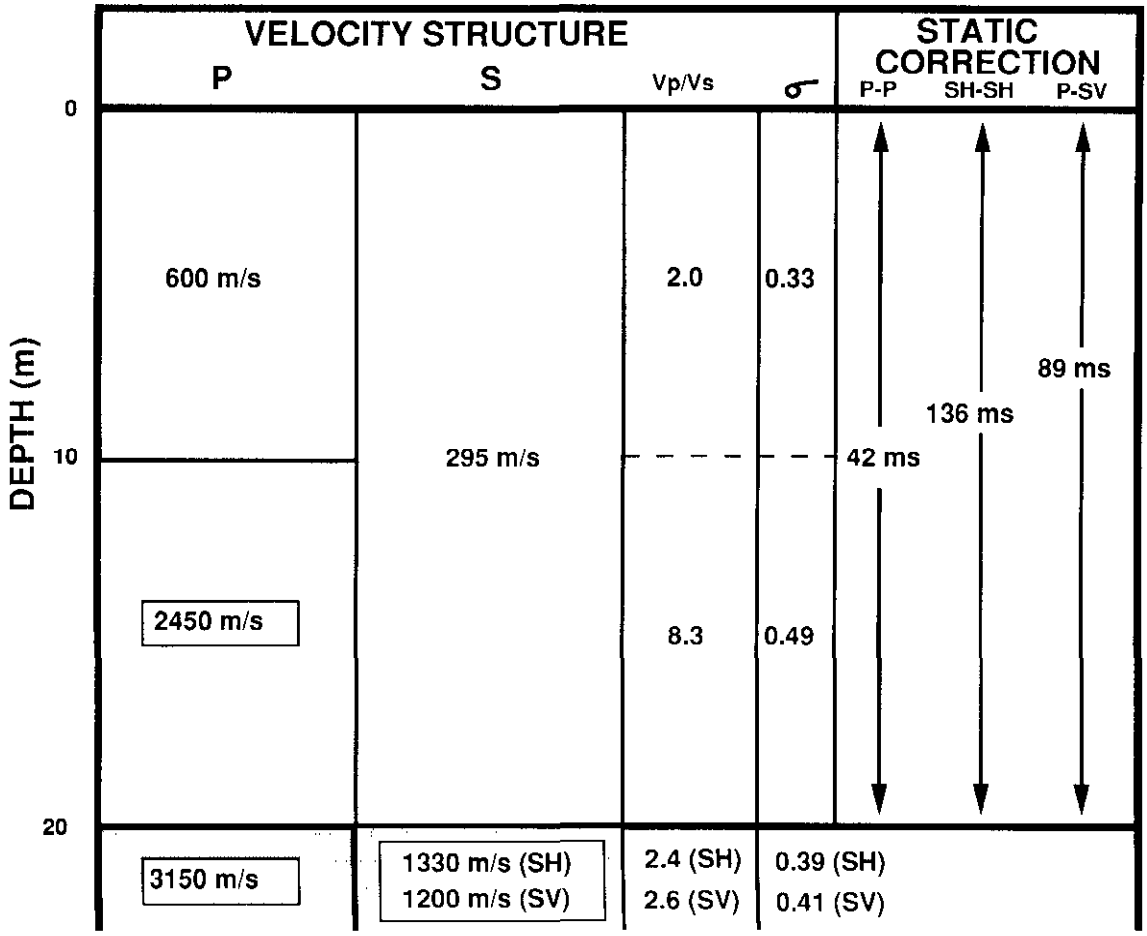

Fig. 9. Summary of the near-surface *P*-wave and *S*-wave depths and velocities.

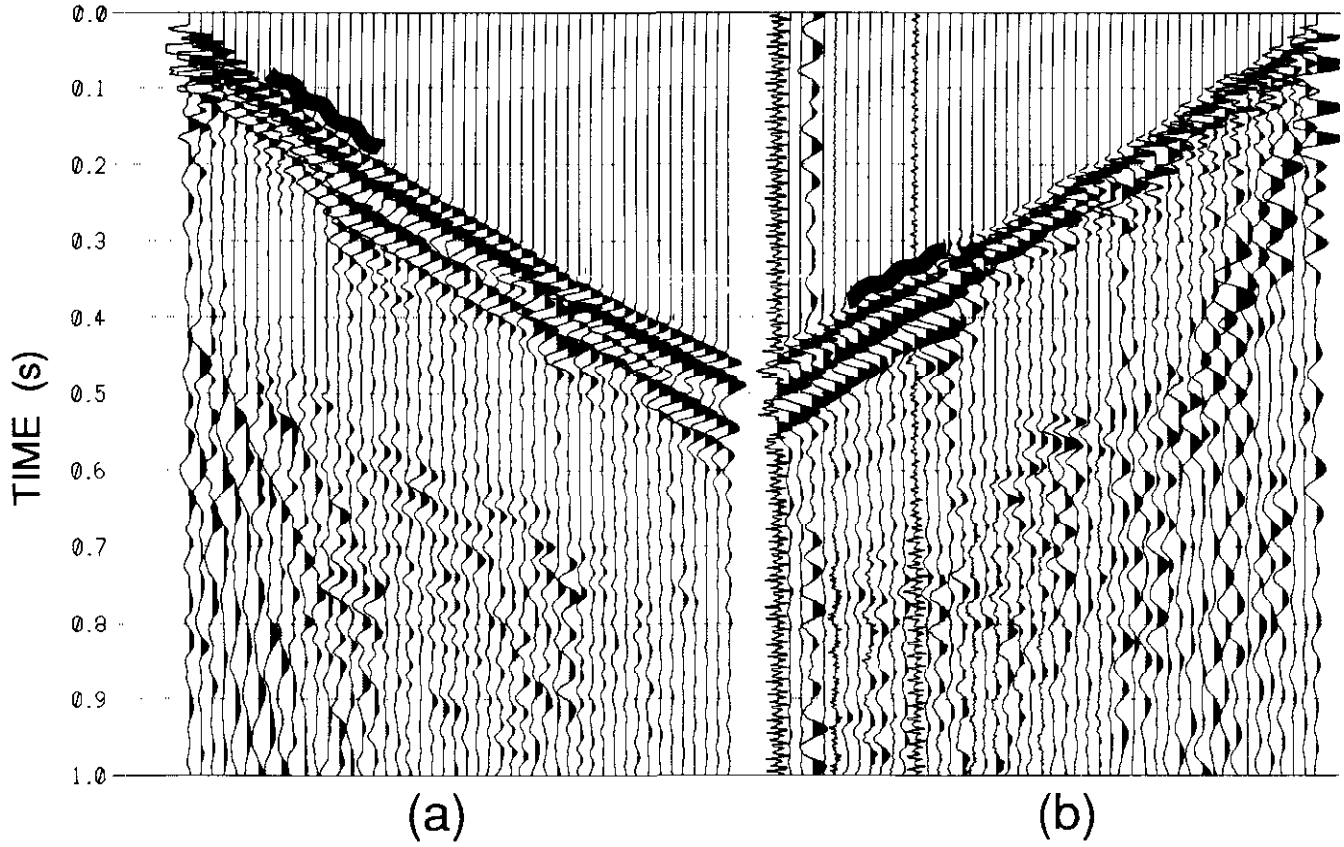

Fig. 10. Reciprocal records from the conventional *P*-wave reflection seismic program. The overlap with the test refraction line is marked on the first breaks, and these data were used to determine the *P*-wave velocity of the subweathering layer and the thickness of the weathering layer below the water table: **(a)** source located at the western end of the spread; **(b)** source located at the eastern end of the spread.

If these differences are not taken into account during the processing of converted *S*-wave data, then the converted-wave reflections will lag the *P*-wave reflections when correlations between vertical and radial-component stacked sections are made.

Conclusions

1. In the study area, the low-velocity layer for *S*-waves is considerably thicker than that for *P*-waves. This is because *S*-waves are unaffected by the water table, whereas the *P*-wave velocity increases markedly at the water table.
2. The *S*-wave velocity of dry, surface sediments is about 295 m/s and the *P*-wave velocity is about 600 m/s.
3. Below the water table (at a depth of about 10 m), the *P*-wave velocity increases to over 2400 m/s while the *S*-wave velocity remains low, resulting in a V_p/V_s of greater than 8.
4. The base of weathering occurs at a depth of about 20 m, for both *P*- and *S*-waves. V_p/V_s for unweathered Cretaceous sediments at the test site is about 2.5.
5. Weak *S*-wave velocity anisotropy was found for the unweathered rocks.
6. Static corrections to a datum at the base of weathering were computed to be 42 ms for *P-P* data, 89 ms for *P-SV* data, and 136 ms for *SH-SH* data.

References

Anno, P.D., 1987, Two critical aspects of shear-wave analysis: statics solutions and reflection correlations, *in* Danbom, S.H. and Domenico, S.N., Eds., Shear-wave exploration: Geophysical development series, Vol. 1, Soc. Expl. Geophys., 48-61.

Chiu, S., and Law, B., 1989, Robust 3-D refraction statics: Can. J. Expl. Geophys. **25**, 85-96.

Domenico, S.N., 1976, Effect of brine-gas mixture on velocity in an unconsolidated sand reservoir: Geophysics **41**, 882-894.

_____ and Danbom, S.H., 1987, Shear-wave technology in petroleum exploration – past, current, and future, *in* Danbom, S.H. and Domenico, S.N., Eds., Shear-wave exploration: Geophysical development series, Vol. 1, Soc. Expl. Geophys., 3-18.

Gardner, L.W., 1939, An areal plan of mapping subsurface structure by refraction shooting: Geophysics **4**, 247-259.

Gregory, A.R., 1976, Fluid saturation effects on dynamic elastic properties of sedimentary rocks: Geophysics **41**, 895-921.

Hagedoorn, J.G., 1959, The plus-minus method for interpreting seismic refraction sections: Geophys. Prosp. **7**, 158-182.

Hampson, D. and Russell, B., 1984, First break interpretation using generalized linear inversion: J. Can. Soc. Expl. Geophys. **20**, 40-54.

Hasbrouk, W.P., 1987, Hammer-impact, shear-wave studies *in* Danbom, S.H. and Domenico, S.N., Eds., Shear-wave exploration: Geophysical development series, Vol. 1, Soc. Expl. Geophys., 97-121.

Hawkins, L.V., 1961, The reciprocal method of routine shallow seismic refraction investigations: Geophysics **26**, 806-819.

Lawton, D.C., 1989, Computation of refraction static corrections using first-break traveltime differences: Geophysics **54**, 1289-1296.

Palmer, D., 1980, The generalised reciprocal method of seismic refraction interpretation: Soc. Expl. Geophys.

Varsek, J.V. and Lawton, D.C., 1985, The seisgun – Part I: field tests: J. Can. Soc. Expl. Geophys. **21**, 77-88.

Wiest, B. and Edelmann, H.A.K., 1984, Static corrections for shear wave sections: Geophys. Prosp. **32**, 1091-1102.